Simulation of airfoil surface pressure due to incident turbulence using realizations of uncorrelated wall plane waves

M. Karimi, P. Croaker, A. Skvortsov, Laurent Maxit, R. Kirby

Simulation of Airfoil Surface Pressure due to Incident Turbulence using Realizations of Uncorrelated Wall Plane Waves

M. Karimi,[1, a)] P. Croaker,[2] A. Skvortsov,[2] L. Maxit,[3] and R. Kirby[1]

[1)] *Centre for Audio, Acoustics and Vibration, University of Technology Sydney, Sydney, Australia*[b)]

[2)] *Maritime Division, Defence Science and Technology, Melbourne, Australia*

[3)] *Univ Lyon, INSA–Lyon, Laboratoire Vibrations-Acoustique (LVA), 25 bis, av. Jean Capelle, F-69621, Villeurbanne Cedex, France*

A numerical technique is proposed for synthesizing realizations of airfoil surface pressure induced by incoming turbulence. In this approach, realization of the surface pressure field is expressed as a set of uncorrelated wall plane waves. The amplitude of these plane waves are determined from the power spectrum density function of the incoming upwash velocity fluctuation and the airfoil aeroacoustic transfer function. The auto spectrum of the surface pressure is obtained from an ensemble average of different realizations. The numerical technique is computationally efficient as it rapidly converges using relatively small number of realizations. The surface pressures for different airfoils excited by incoming turbulence are numerically predicted and the results are compared with experimental data in literature. Further, the unsteady force exerted on an airfoil due to the airfoil-turbulence interaction is also computed and it is shown to be in very good agreement with analytical results.

[a)] Mahmoud.karimi@uts.edu.au

[b)] Also at: School of Mechanical and Manufacturing Engineering, UNSW Sydney, Australia

I. INTRODUCTION

The noise generated from interaction of incoming turbulence with an airfoil occur in many industrial applications, and has been studied by many researchers in the literature. The interaction between an airfoil and incoming turbulence induces lift fluctuations which radiates noise to the far field as acoustic dipoles. A turbulent flow field can be formed upstream of an airfoil due to the presence of inflow distortions and/or other aerodynamic elements. When there is also a steady inflow, a turbulent flow can be produced by the development of a turbulent boundary layer over the airfoil surface. These noise generation mechanism are respectively called as leading edge noise (incoming turbulence noise) mechanism (Amiet, 1975, 1976b; Ayton and Chaitanya, 2017; Ayton and Peake, 2016; Paterson and Amiet, 1976) and trailing edge noise (self noise) mechanism (Amiet, 1976a, 1978; Brooks, 1981; Moreau *et al.*, 2008). These two mechanisms can be present at the same time. Nevertheless, if the turbulence intensity of incoming flow field is large enough, the pressure fluctuations associated with boundary layer eddies will be small compared with the unsteady pressure due to the incoming turbulence. In this case the turbulence ingestion noise becomes the predominant noise (Moreau and Roger, 2007).

The leading edge noise has been extensively studied both numerically and experimentally (Amiet, 1975; de Santana *et al.*, 2015; Devenport *et al.*, 2010; Glegg and Devenport, 2010; Hutcheson *et al.*, 2012; Mish and Devenport, 2006a; Paterson and Amiet, 1976; Roger and Moreau, 2010). Paterson and Amiet (1976) theoretically and experimentally investigated the noise and unsteady surface pressure of a NACA0012 airfoil in a grid generated turbulence. They considered a free stream Mach number range of 0.1 to 0.5. Unsteady airfoil surface pressure spectra and

surface pressure cross-spectra were obtained in both spanwise and chordwise distribution in an anechoic chamber that surrounded the tunnel open jet test section. A reasonable agreement between measured and predicted surface pressure spectra at zero angle of attack was achieved. A good agreement between Amiet's far-field predictions and far field measurements was also observed (Amiet, 1975). Mish (2001); Mish and Devenport (2003) investigated the response of an airfoil to the incoming turbulence. The mean loading effects on the response of the airfoil encountering turbulence was experimentally studied (Mish and Devenport, 2006a). Measured pressure on the surface of a NACA 0015 immersed in grid turbulence indicated a reduction of up to 5 dB with increasing angle of attack for reduced frequencies less than 5. It was demonstrated that Amiet's method not only works for zero angle of attack but also it can be used for predicting the airfoil response at small angle of attack.

A detailed measurements of turbulent flow generated by either a grid or a rod interacting with NACA 0012 airfoil was conducted by a de Santana *et al.* (2015). They used stereoscopic particle image velocimetry as well as hot wire anemometry in the experiment. The focus of the study was on quantification of turbulence distortion. This was done by measuring the turbulence properties in the vicinity of the leading edge. It was found that even when the flow in the spanwise direction is almost homogenous, in order to improve the sound prediction small variations have to be considered. Hutcheson *et al.* (2012) experimentally studied the radiated leading edge noise of an airfoil immersed in nearly isotropic turbulence. It was shown that at zero angle of attack, the airfoil's thickness and chord play an important role in controlling the spectral peak level. Further, an increase in turbulence intensity and integral scale resulted in a uniform increase of the noise levels. Previously proposed analytical models in the literature to predict the broadband noise generated

by thin airfoils in a turbulent flow were reviewed by Roger and Moreau (2010). Three generating mechanisms were examined, the turbulence-interaction noise (leading edge noise), turbulent boundary layer noise (trailing edge noise), and vortex shedding noise (near wake of a thick trailing edge). The models for noise prediction in all these cases were experimentally validated for thin airfoils and the limitations and assumptions behind the development of the models were discussed.

Most of the previous studies focused on noise prediction of a rigid airfoil in turbulent flow disregarding elasticity of the structure (Amiet, 1975; de Santana *et al.*, 2015; Mish, 2001). However, in practice airfoils are made of elastic materials, therefore the surface pressure jump can excite the airfoil and cause vibration and this vibration radiates noise to the far field. Neglecting this radiated noise might be justifiable in air, as the aeroelastic coupling between the airfoil and air is quite weak. However, for an airfoil in water, where the fluid-structure coupling is strong, vibroacoustic contribution to the radiated noise can be significant. To study this vibroacoustic contribution, element-based vibroacoustic models can be employed to estimate the radiated noise by the elastic structure under incoming turbulence excitation. The main challenge of this framework is that the element-based models require deterministic loads whereas the incoming turbulence is non-deterministic by its nature and described by stochastic models. In other words, due to the random nature of incoming turbulence, the surface pressure can be characterized by statistical parameters such as auto spectrum density (ASD) or cross spectrum density (CSD) that can be obtained using stochastic models. However, in an element-based model such as the finite element model, airfoil surface is discretized by finite elements and deterministic nodal forces are required to obtain the vibroacoustic response. To overcome this challenge, we have proposed an efficient numerical technique to synthesize realizations of deterministic surface pressure produced by incoming

turbulence. The proposed technique can be easily implemented in any finite element or boundary element software.

The uncorrelated wall plane wave (UWPW) technique has recently been used to synthesize the wall pressure field underneath a turbulent boundary layer by some of the authors (Karimi *et al.*, 2020, 2019a,b; Maxit, 2016). This method which is based on representing a stochastic field by superposition of uncorrelated wall plane waves is extended here to synthesize the surface pressure from incoming turbulence. This approach is conceptually similar to stochastic noise generation and radiation (SNGR) method (Bechara *et al.*, 1994; Kraichnan, 1970) which is one of the promising approaches often applied in synthetic turbulence modeling. The SNGR method expresses the turbulence velocity field as a superposition of time-harmonic plane waves (Fourier modes), where mode amplitudes and random phases are chosen in such a way to match the properties of the turbulent flow. Employing the same concept herein, a formulation has been proposed to simulate the pressure fluctuations on an airfoil interacting with an incoming turbulent flow. Realizations of the unsteady surface pressure jump from incoming turbulence are expressed as a set of uncorrelated plane waves traveling in the spanwise direction. The amplitudes of the waves are defined such that the CSD of the UWPWs approximates the CSD of the pressure field induced by the turbulence ingestion. Therefore, the amplitudes of the waves become dependent on the power spectrum density function of the incoming upwash velocity fluctuation and the airfoil aeroacoustic transfer function. To generate uncorrelated waves, the phases of the plane waves are randomly chosen from a uniform distribution between 0 and 2 π. The predicted auto spectrum of the surface pressure jump is then obtained by ensemble average over different realizations. The effect of the number of realizations and cut-off wavenumber on the predicted surface pressure jump is investigated.

Numerical results are compared with available experimental data from literature, showing very good agreement. Although the focus of the current study is on simulation of the surface pressure jump and demonstration of validity of the proposed method, to show how the deterministic surface pressure jump can be employed to perform further analysis, the unsteady force acting on an airfoil is also predicted using the UWPW technique, and numerical results are verified against analytical results. To the best knowledge of the authors, this is the first time that the surface pressure jump induced by airfoil-turbulence interaction is deterministically synthesized.

II. AIRFOIL-TURBULENCE INTERACTION MODEL

Amiet (1975) developed a model to describe airfoil-turbulence interaction and the resulting noise production. Amiet's model is based on linearized thin-airfoil theory, and the airfoil is represented by a flat plate of a zero thickness and assumed to be at zero angle of attack (Lysak, 2001). The model is based on several assumptions:

- The incoming turbulence fluctuation is considered to be small compared to the mean flow velocity. This enables us to employ the small perturbation theory and to linearize the aerodynamic response.

- The turbulent flow is assumed to be inviscid so that the problem is reduced to solving linearized Euler equations.

- The turbulence is frozen so that turbulent gust properties are not altered when it is convected by the mean flow.

Amiet's formulation is summarized in this section for an airfoil of chord $2b$ and span $2d$ in a turbulent flow with a mean flow U_∞ in the x-direction, as shown in Figure 1. The airfoil is located in the plane $z = 0$. The y-coordinate extends in the spanwise direction, and the origin of the coordinate system is at the leading edge of the airfoil. To analyze the gust-airfoil problem, the Helmholtz

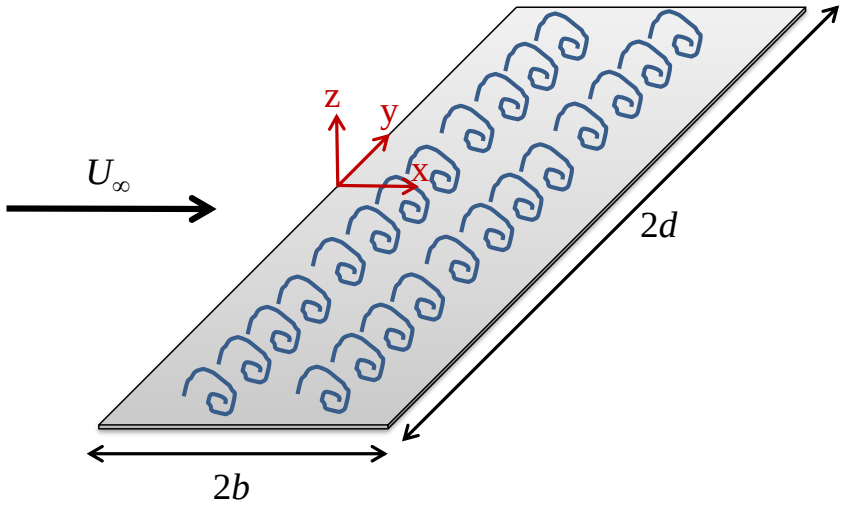

FIG. 1. (color online) Schematic diagram of airfoil-gust interaction.

equation along with three boundary conditions need to be solved. To deal with this problem, an iterative procedure was proposed by Amiet (Amiet, 1975, 1976b). In this three-step procedure each boundary equation is solved in each iteration. First, the Helmholtz equation is solved for the aerodynamic gust interacting with an infinite flat plate with a non-penetration boundary condition. The non-penetration boundary condition and a zero flow potential condition are then imposed upstream of the leading edge and the problem is solved using the Schwarzschild theorem. In the final iteration, this theorem is used to find a solution for the problem by considering a zero pressure jump and the Kutta conditions as well as non-penetration boundary equation downstream of the trailing edge.

The upwash velocity perturbation is convected with the uniform velocity U_∞, and can thus be written as a spatial Fourier decomposition as follows (Amiet, 1975; de Santana *et al.*, 2015)

$$w(x,y,t) = \int_{-\infty}^{\infty}\int_{-\infty}^{\infty} \widetilde{w}(k_x,k_y) e^{\mathrm{i}(k_x(x-U_\infty t)+k_y y)} dk_x dk_y, \tag{1}$$

where $\mathrm{i} = \sqrt{-1}$ is the imaginary unit, and k_x, k_y are the wavevector components in the streamwise and spanwise directions, respectively. The Fourier components $\widetilde{w}(k_x,k_y)$ are defined as:

$$\widetilde{w}(k_x,k_y) = \frac{1}{4\pi^2}\int_{-\mathrm{R}}^{\mathrm{R}}\int_{-\mathrm{R}}^{\mathrm{R}} w(x,y) e^{\mathrm{i}(k_x x+k_y y)} dx dy, \tag{2}$$

the turbulence was assumed to be extended in the area of $-R < \{x,y\} < R$. R is not set equal to infinity because of convergence difficulties if $w(x,y)$ does not go to zero as x and y go to infinity. The pressure jump at a given point on the airfoil due to all wavenumber components is given by (Amiet, 1975; de Santana *et al.*, 2015; Santana *et al.*, 2016)

$$\Delta p(x,y,t) = 2\pi\rho U_\infty \int_{-\infty}^{\infty}\int_{-\infty}^{\infty} \widetilde{w}(k_x,k_y) g(x,k_x,k_y) e^{\mathrm{i}(k_x(x-U_\infty t)+k_y y)} dk_x dk_y, \tag{3}$$

where ρ is fluid density and $g(x,k_x,k_y)$ is the transfer function between the incoming gust velocity perturbation $\widetilde{w}(k_x,k_y)$ and the airfoil pressure jump at the chordwise coordinate x. The Fourier transform with respect to time of Equation (3) yields (Amiet, 1975; de Santana *et al.*, 2015)

$$\Delta p(x,y,\omega) = 2\pi\rho \int_{-\infty}^{\infty} \widetilde{w}(K_x,k_y) g(x,K_x,k_y) e^{\mathrm{i}(k_y y)} dk_y, \tag{4}$$

where $K_x = \omega/U_\infty$ is the convective wavenumber and $\omega = 2\pi f$ is the angular frequency. For broadband noise problems, $\widehat{w}(K_x,k_y)$ is considered as a non-deterministic quantity (Amiet, 1975,

1978). The single-sided CSD of the pressure jump at two points on the airfoil surface is given by (de Santana *et al.*, 2015; Mish and Devenport, 2006a)

$$S_{\Delta p\Delta p}(x,x',y,y',f) = 16\pi(\pi\rho)^2 U_\infty \int_0^\infty \phi_{ww}(K_x,k_y) g^*(x,K_x,k_y) g(x',K_x,k_y) e^{\mathrm{i}(k_y(y-y'))} dk_y, \tag{5}$$

ϕ_{ww} is the single-sided power spectrum density of the incoming upwash velocity fluctuation and based on the von Karman isotropic model can be written as (Amiet, 1975; de Santana *et al.*, 2015)

$$\phi_{ww}(K_x,k_y) = \frac{4u'^2}{9\pi k_e^2} \frac{\underline{K}_x^2 + \underline{k}_y^2}{(1+\underline{K}_x^2+\underline{k}_y^2)^{7/3}}, \tag{6}$$

where u' is turbulence intensity, $\underline{k} = k/k_e$, $k_e = (\sqrt{\pi}/\Lambda_f)\Gamma(5/6)/\Gamma(1/3)$, Λ_f is the turbulence integral length scale and Γ represents the Gamma function. It has been reported that depending on the distance to the leading edge, the turbulence spectrum shows two different decay slopes at high frequencies. For long distances, one can apply von Karman isotropic model given by Equation (6) (for more details please see Christophe (2011); de Santana *et al.* (2015)). However, for short distances a modified von Karman spectrum applies which is based on the rapid distortion theory and is given by (de Santana *et al.*, 2015; Hunt, 1973)

$$\phi_{ww}(K_x,k_y) = \frac{91u'^2}{36\pi k_e^2} \frac{\underline{K}_x^2 + \underline{k}_y^2}{(1+\underline{K}_x^2+\underline{k}_y^2)^{19/6}}. \tag{7}$$

Amiet (1976b) derived solutions for the pressure and lift of a flat plat in incident turbulence by modifying Filotas' work (Filotas, 1969). This complete solution consists of two solution regions. One region is valid for small spanwise wavenumbers k_y (super-critical gust) and the other region for large spanwise wavenumbers (sub-critical gust) giving essentially a complete low to high

frequency solution to the problem of a flat-plate airfoil encountering a skewed gust. The airfoil transfer function g associated with these two solution regions was derived by Mish (Mish, 2001; Mish and Devenport, 2006a) as follows

$$g(x, K_x, k_y) = -\frac{\Xi(x, K_x, k_y)}{\pi\beta}\left(\pi x\left(\left(\frac{k_y^2}{\beta^2} - \mu^2\right)^{\frac{1}{2}} + \mathrm{i}\left(\mu M + K_x\right)\right)\right)^{-\frac{1}{2}} e^{\mathrm{i}\mu M x - x\left(\frac{k_y^2}{\beta^2} - \mu^2\right)^{\frac{1}{2}}}, \tag{8}$$

if $k_y \geq (M/\beta)K_x$

$$\Xi(x, K_x, k_y) = 1 - \left(\frac{x}{2b}\right)^{\frac{1}{2}}\left[1 - \mathrm{erf}\left(\left(2b\left(2 - \frac{x}{b}\right)\left(\frac{k_y^2}{\beta^2} - \mu^2\right)^{\frac{1}{2}}\right)^{\frac{1}{2}}\right)\right], \tag{9}$$

if $k_y < (M/\beta)K_x$

$$\Xi(x, K_x, k_y) = 1 - \left(\frac{x}{2b}\right)^{\frac{1}{2}}\left[1 - (1 - \mathrm{i})\,\mathfrak{F}\left(2\mathrm{i}\left(\frac{b}{\pi}\left(2 - \frac{x}{b}\right)\left(-\frac{k_y^2}{\beta^2} + \mu^2\right)^{\frac{1}{2}}\right)^{\frac{1}{2}}\right)\right]. \tag{10}$$

In these equations, M is the Mach number, $\beta = \sqrt{1 - M^2}$, $\mu = MK_x/\beta^2$, erf( ) is the Error function, and $\mathfrak{F}(\ )$ is a combination of Fresnel integrals function and are given by

$$\mathrm{erf}(z) = \frac{2}{\sqrt{\pi}}\int_0^z e^{-t^2}dt, \tag{11}$$

$$\mathfrak{F}(z) = C(z) + \mathrm{i}S(z), \tag{12}$$

where $C(z)$ and $S(z)$ are respectively Fresnel cosine and sine integral functions

$$C(z) = \int_0^z \cos(\frac{\pi}{2}t^2)dt, \quad \text{and} \quad S(z) = \int_0^z \sin(\frac{\pi}{2}t^2)dt, \tag{13}$$

assuming $z = 2(\frac{b}{\pi}(2 - \frac{x}{b})(-\frac{k_y^2}{\beta^2} + \mu^2)^{\frac{1}{2}})^{\frac{1}{2}}$, the Fresnel integrals in Equation (10) can be written as follows

$$\mathfrak{F}(\mathrm{i}z) = \left\{ \begin{array}{ll} S(z)\text{+i } C(z) & \text{if } \ z \geq 0, \\ \\ \text{-}S(z)\text{-i } C(z) & \text{if } \ z \leq 0, \end{array} \right\}, \tag{14}$$

To reduce the computation time, one can avoid evaluating the integrals in the Fresnel functions by exploiting approximate functions. $C(z)$ and $S(z)$ can be rewritten in terms of auxiliary functions $\Psi(z)$ and $\Phi(z)$ (Abramowitz and Stegun, 1948)

$$C(z) = \frac{1}{2} + \Psi(z)\sin(\frac{\pi}{2}z^2) - \Phi(z)\cos(\frac{\pi}{2}z^2), \tag{15}$$

$$S(z) = \frac{1}{2} - \Psi(z)\cos(\frac{\pi}{2}z^2) - \Phi(z)\sin(\frac{\pi}{2}z^2), \tag{16}$$

where the auxiliary functions can be approximated by

$$\Psi(z) = \frac{1 + 0.926z}{2 + 1.792z + 3.104z^2} + \epsilon(z), \qquad |\epsilon(z)| \leq 2 \times 10^{-3}, \tag{17}$$

$$\Phi(z) = \frac{1}{2 + 4.142z + 3.492z^2 + 6.670z^3} + \epsilon(z), \qquad |\epsilon(z)| \leq 2 \times 10^{-3}, \tag{18}$$

$\epsilon(z)$ represents the error in using these approximate functions.

III. UNCORRELATED WALL PLANE WAVE TECHNIQUE

The uncorrelated wall plane wave technique was initially introduced by Maxit (2016) to simulate the pressure field beneath a turbulent boundary layer using realizations of UWPWs. This

technique has been extended to simulate the pressure jump on the airfoil, which can be expressed as a set of uncorrelated wall plane waves traveling in the y-direction for the n^{th} realization as follows

$$(\Delta p^n(x,y,f))_{\text{UWPW}} = \sum_{i=1}^{N} A(x,k_y^i,f)e^{\mathrm{i}(k_y^i y+\varphi_i^n)}, \tag{19}$$

where A^i are the stochastic amplitudes of the UWPWs, N represents the number of UWPWs and φ is a random phase uniformly distributed in $[0\ \ 2\pi]$. It should be noted that these wall plane waves are surface waves as they are only defined at the surface of the structure. Further, unlike the original version of the UWPW technique which was developed to synthesize wall pressure underneath a turbulent boundary layer (Maxit, 2016), the plane waves here are only traveling in the y-direction and their amplitudes varies along the x-direction. It can be shown that the cross spectrum of the surface pressure jump is given by

$$(S_{\Delta p\Delta p}(x,x',y,y',f))_{\text{UWPW}} = \mathrm{E}\left[\sum_{i=1}^{N} A(x,k_y^i,f)e^{\mathrm{i}(k_y^i y+\varphi_i^n)} \times \overline{\sum_{j=1}^{N} A(x',k_y^j,f)e^{\mathrm{i}(k_y^j y'+\varphi_j^n)}}\right], \tag{20}$$

where E[ ] represents the ensemble average over the realizations and the upper bar denotes the complex conjugate of the complex number. Equation (20) can be rewritten as follows

$$(S_{\Delta p\Delta p}(x,x',y,y',f))_{\text{UWPW}} = \sum_{i=1}^{N}\sum_{j=1}^{N} \mathrm{E}\left[A(x,k_y^i,f)A^*(x',k_y^j,f)\right] e^{\mathrm{i}(k_y^i y-k_y^j y')}\mathrm{E}\left[e^{\mathrm{i}(\varphi_i^n-\varphi_j^n)}\right], \tag{21}$$

where

$$\mathrm{E}\left[e^{\mathrm{i}(\varphi_i^n-\varphi_j^n)}\right] = \begin{cases} 1 & i=j \\ 0 & \text{otherwise} \end{cases}, \tag{22}$$

196 therefore

$$(S_{\Delta p\Delta p})_{\text{UWPW}} = \sum_{i=1}^{N} \mathrm{E}\left[A(x, k_y^i, f)A^*(x', k_y^i, f)\right] e^{\mathrm{i}(k_y^i(y-y'))}. \tag{23}$$

197 Revisiting Equation (5), the improper integral can be approximated using the rectangular rule by
198 truncating and regularly sampling the wavenumber space as follows

$$S_{\Delta p\Delta p} \approx 16\pi(\pi\rho)^2 U_\infty \sum_{i=1}^{N} \phi_{ww}(K_x, k_y^i) g^*(x, K_x, k_y^i) g(x', K_x, k_y^i) e^{\mathrm{i}(k_y^i(y-y'))} \delta k_y^i, \tag{24}$$

199 comparing equations (23) and (24), it can be concluded that the CSD of the pressure field by the
200 turbulence ingestion is approximately equal to the CSD of the UWPWs if the amplitudes of the
201 UWPWs in Equation (19) are defined by

$$A(x, k_y^i, f) = 4\pi\rho g(x, K_x, k_y^i)\sqrt{\pi U_\infty \phi_{ww}(K_x, k_y^i)\delta k_y^i}. \tag{25}$$

202 In fact, the amplitude of each wall pressure plane wave is defined such that the whole set can repre-
203 sent the statistical properties of a pressure jump generated by incoming gust. The final expression
204 of the n^{th} realization of surface pressure jump on the airfoil using the UWPW technique can be
205 obtained by

$$\Delta p^n(x, y, f) = 4\pi\rho \sum_{i=1}^{N} g(x, K_x, k_y^i)\sqrt{\pi U_\infty \phi_{ww}(K_x, k_y^i)\delta k_y} e^{\mathrm{i}(k_y^i y + \varphi_i^n)}, \tag{26}$$

206 The surface pressure jump is varying spatially in the spanwise direction as $e^{\mathrm{i}(k_y^i y)}$ while its variation
207 in the streamwise direction is governed by the transfer function. The auto spectrum density (ASD)
208 of the surface pressure jump $S_{\Delta p\Delta p}$ due to the incident turbulence is then calculated from the

ensemble average of different realizations by

$$S_{\Delta p \Delta p}(x, y, f) = \mathrm{E}\left[\Delta p^n(x, y, f) \Delta p^{*n}(x, y, f)\right], \tag{27}$$

This process is repeated for each frequency to obtain the spectra of the surface pressure jump. Once the surface pressure jump is available, realizations of unsteady force acting on the airfoil surface can also be obtained by integrating the pressure jump over the airfoil surface (represented by a flat plate) as follows

$$F^n(f) = \int_{-d}^{d} \int_{0}^{2b} \Delta p^n(x, y, f) dx dy, \tag{28}$$

Accordingly, the ASD of the unsteady force S_{FF} is calculated from the ensemble average of different realizations by

$$S_{FF}(f) = \mathrm{E}\left[F^n(f) F^{*n}(f)\right]. \tag{29}$$

It should be noted the surface pressure (p_s) is related to pressure jump by $|p_s| = |\Delta p| / 2$. The technique developed in this work is based on the assumption that the surface pressure field induced by incoming turbulence is not altered by the vibration of the airfoil. The proposed method enables us to estimate the unsteady surface pressure jump (loads) on an airfoil due to turbulence interaction as deterministic excitations, these excitations can then be applied to element-based vibroacoustic analysis techniques. The proposed technique allows that the statistical model to describe the surface pressure fluctuations to be coupled with deterministic and element-based numerical methods such as the finite element and boundary element methods to investigate the vibroacoustic behavior of airfoils in turbulent flow.

IV. NUMERICAL RESULTS

In this section the UWPW technique has been implemented in Matlab to synthesize the surface pressure jump for two different airfoil models of varying chord length and flow speed as listed in Table 1. The first airfoil (Case 1) corresponds to the experiments performed at the Virginia Tech Stability Wind Tunnel (Mish and Devenport, 2006a,b). The unsteady surface pressure jump was measured on a NACA0015 airfoil with 0.610 m chord and 1.83 m span at flow speed of 30 m/s. This airfoil is used for all the numerical investigations in this work unless stated otherwise. The second airfoil (Case 2) is a NACA0012 with a chord of $0.230\,\mathrm{m}$ and span of $0.530\,\mathrm{m}$ which was tested by Paterson and Amiet (1976) and it has been used in this work to further validate the proposed method.

TABLE I. Input parameters used in the prediction code for each case study

Case	Airfoil	Flow speed (m/s)	Integral length scale Λ_f (m)	Turbulence intensity u'/U_∞
1	NACA0015	30	0.0818	0.0398
2	NACA0012	40	0.0302	0.0453
		60	0.0301	0.0392
		90	0.0294	0.0482
		120 and 165	0.0305	0.0414

A. Cutoff wavenumber and wavenumber resolution

To correctly approximate the improper integral in Equation (5), criteria for choosing the cut-off wavenumber and wavenumber resolution need to be defined in the spanwise direction. Fig-

ure 2 (a) presents the square of the transfer function modulus in the wavenumber domain. The dashed line corresponds to $k_y = (M/\beta)K_x$ which splits the wavenumber domain into two regions. The region where $k_y < (M/\beta)K_x$ is associated with super-critical gust while the region where $k_y \geq (M/\beta)K_x$ contains the sub-critical gusts. According to Figure 2 (a) when the convective wavenumber is almost below 4000 m^{-1}, the highest values of the transfer function occurs for spanwise wavenumbers k_y <200 m^{-1} and the contributions of both sub-critical or super-critical gusts are significant. At higher convective wavenumbers (or higher frequencies) only those wavenumbers corresponding to the super-critical gusts are important and the effect of sub-critical gust can be neglected. Figure 2 (b) shows the color map of the modified von Karman spectrum. The values of the function $\phi_{ww}(K_x, k_y)$ is insignificant for convective wavenumbers larger than 700 m^{-1}. Below this convective wavenumber, the values of the function is considerable for spanwise wavenumbers k_y <900 m^{-1}. It should be noted that to find the effective range of wavenumbers for calculation of surface pressure jump we need to inspect the integrand of the integral in Equation (5). Determination of the cutoff wavenumber can be achieved by plotting the integrand which is the product of the square of the transfer function modulus (Figure 2 (a)) and von Karman spectrum (Figure 2 (b)). Figure 2 (c) presents the color map of the integrand. As illustrated in this figure, the Graham's parameter ($\Theta = MK_x/(\beta k_y)$) of less than or greater than unity corresponds respectively to sub-critical or super-critical gusts (Karimi *et al.*, 2019a). Figure 2 (c) reveals that at very low frequencies, contributions of sub-critical wavenumbers are dominant. However, as frequency increases, the super-critical gusts have an increasing contribution to the incoming turbulence pressure to the point where above $K_x \approx 400\ m^{-1}$ they become the

dominant contribution. The significance of these contributions to the predicted surface pressure jump over frequency range is further investigated in Section IV D.

To take into account the significant contributions of the integrand, the following cut-off wavenumber is selected: k_y^{co}=70 m^{-1} for $K_x \leq 700$ m^{-1} and $k_y^{\text{co}} = MK_x/\beta$ when $K_x > 700$ m^{-1}. This criterion for cut-off wavenumber was achieved by ensuring that the maximum estimated error in the calculation of the surface pressure jump associated with the wavenumber domain truncation was less than 1 dB for the frequency range. A trial and error process was also conducted to find a wavenumber resolution which correctly represent the spatial variations of the integrand in the wavenumber space. It was found that a constant wavenumber resolution of δk_y=0.1 m^{-1} is a good choice.

B. Number of realizations

The effect of the number of realizations on the accuracy of the UWPW technique was evaluated as follows. The result obtained using 500 realizations was selected as a converged solution and used as a reference to compute the discrepancy (Δ) between results obtained with different numbers of realizations. The discrepancy is shown in Figure 3 for 10, 30, 50, 80 and 100 realizations. For the current case study, the maximum error using 10, 30, 50, 80 and 100 realizations over the frequency range are approximately 5.2 dB, 2.1 dB, 1.7 dB. 1.5 dB and 1.4 dB. A suitable number of realizations can be selected depending on the required accuracy. In this work, for all the calculations 50 realizations have been considered in the UWPW technique. Figure 4 shows the ASD of the surface pressure jump as a function of reduced frequency ($\omega_r = \omega b/U_\infty$) at 6% chord. The spectral level predicted using 50 different realizations is shown in gray lines and the

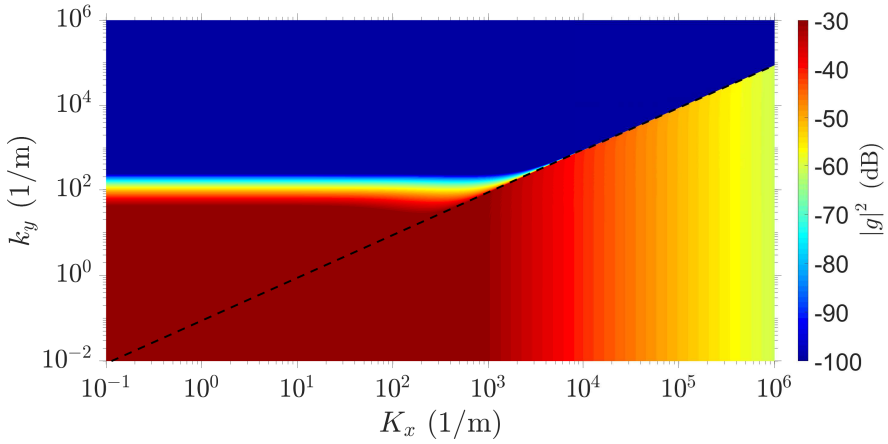

(a)

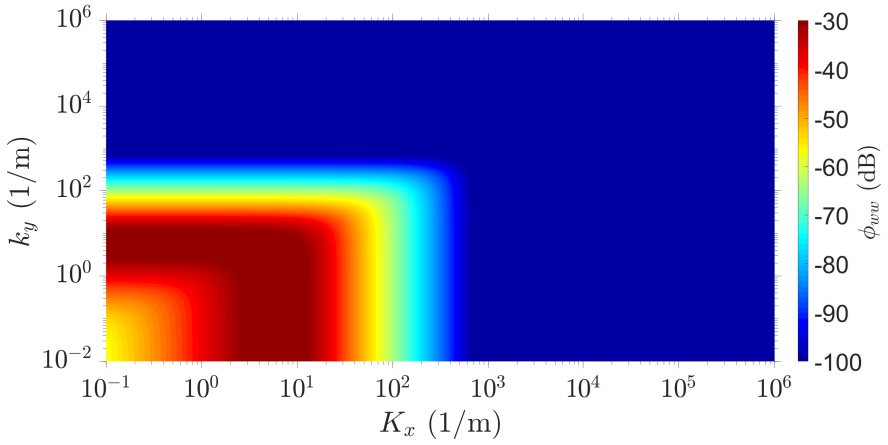

(b)

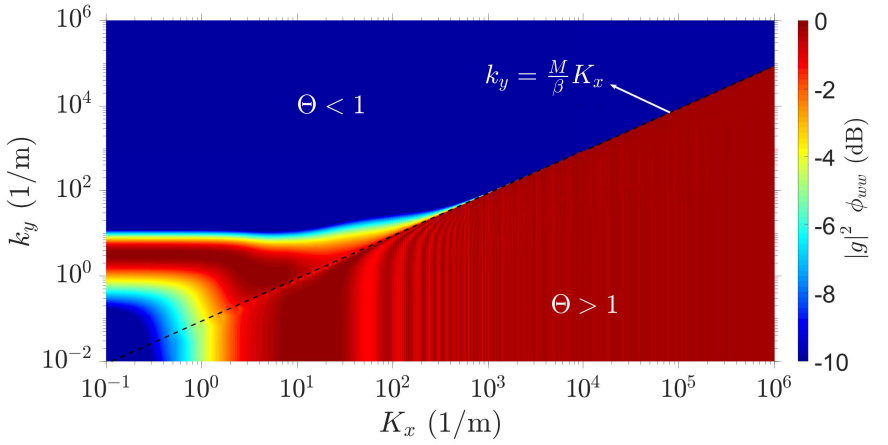

(c)

FIG. 2. (color online) Color maps of the (a) airfoil transfer function $|g(x, K_x, k_y)|^2$ (dB, ref. 1), (b) modified von Karman spectrum $\phi_{ww}(K_x, k_y)$ (dB, ref. 1 $\mathrm{m^2 s^{-2} Hz^{-1}}$), and (c) integrand obtained by the product of (a) and (b) normalized by the maximum value at each convective wavenumber (dB, ref. 1 $\mathrm{m^2 s^{-2} Hz^{-1}}$). The dashed line in (a) and (c) corresponds to the Graham's parameter showing critical gusts $\Theta = 1$, which separates sub-critical gusts ($\Theta < 1$) from super-critical gusts ($\Theta > 1$).

black line represents the predicted results by averaging of 50 realizations. It can be observed from Figures 3 and 4 that the numerical results become smoother and converge quickly by increasing the number of realizations.

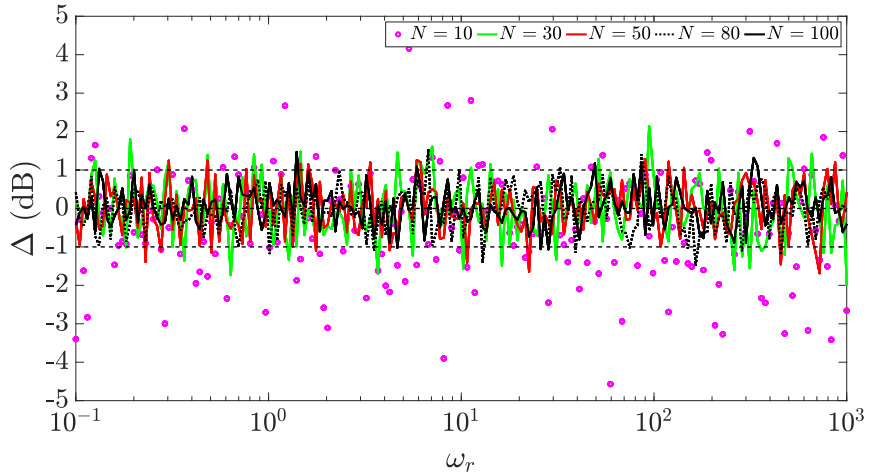

FIG. 3. (color online) Difference in the spectral level of the surface pressure jump for different numbers of realizations using the results obtained with 500 realizations as the reference solution, (dB, ref. $4 \times 10^{-10}\mathrm{Pa}^2/\mathrm{Hz}$).

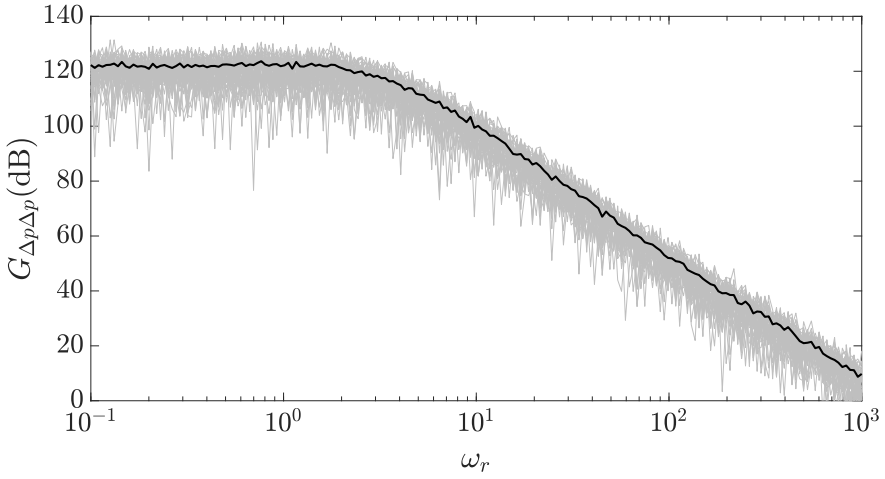

FIG. 4. ASD of the surface pressure jump predicted numerically using the UWPW technique for 50 realizations (gray lines), as well as predicted using the average of 50 realizations (black line), (dB, ref. $4 \times 10^{-10}\mathrm{Pa}^2/\mathrm{Hz}$).

C. Statistics of the synthesized surface pressure jump

As stated in Section III, the surface pressure jump can be obtained using the UWPW technique from summation of uncorrelated plane waves with a random phase uniformly distributed in $[0 \;\; 2\pi]$ as given by Equation (19). If the amplitudes of the waves were independent of k_y, each plane wave would be an independent and identically distributed random variable. In such a case, according to the central limit theorem (CLT) as N approaches infinity the sum of these independent random variables tends toward a normal distribution. Moreover, since $\mathrm{E}\left[e^{\mathrm{i}(\varphi_i^n)}\right] = 0$ (see Equation (19)), the mean value of the plane wave contributions would be zero. However, in the present case, the wave amplitudes are a function of k_y and the CLT may not be rigorously valid. Figure 5 presents the probability density function (PDF) of the real and imaginary parts of synthesized surface pressure jump using 500 realizations at $\omega_r = 1$. In spite of the fact that the wave amplitudes are dependent on k_y, it can be observed that the PDF of the real and imaginary parts of the pressure jump generated by the UWPW technique follows the normal distribution with a mean value of zero. Further, variance of the synthesized pressures equals the sum of the variances of the real and imaginary part of these pressures which corresponds to the targeted ASD of the pressure jump. Targeted ASD can be obtained from Equation (24) by considering $x = x'$ and $y = y'$. For the current case shown in Figure 5, variances of the real and imaginary parts of the pressures are respectively 22.52 Pa^2 and 22.35 Pa^2. Therefore, variance of the complex synthesized pressures is 44.87 Pa^2 which corresponds to the targeted ASD of the pressure jump with a value of 45.42 $\mathrm{Pa}^2/\mathrm{Hz}$. It should be noted that the estimated ASD of the pressure jump using 500 realizations is 45.53 $\mathrm{Pa}^2/\mathrm{Hz}$ which is very close to the targeted ASD.

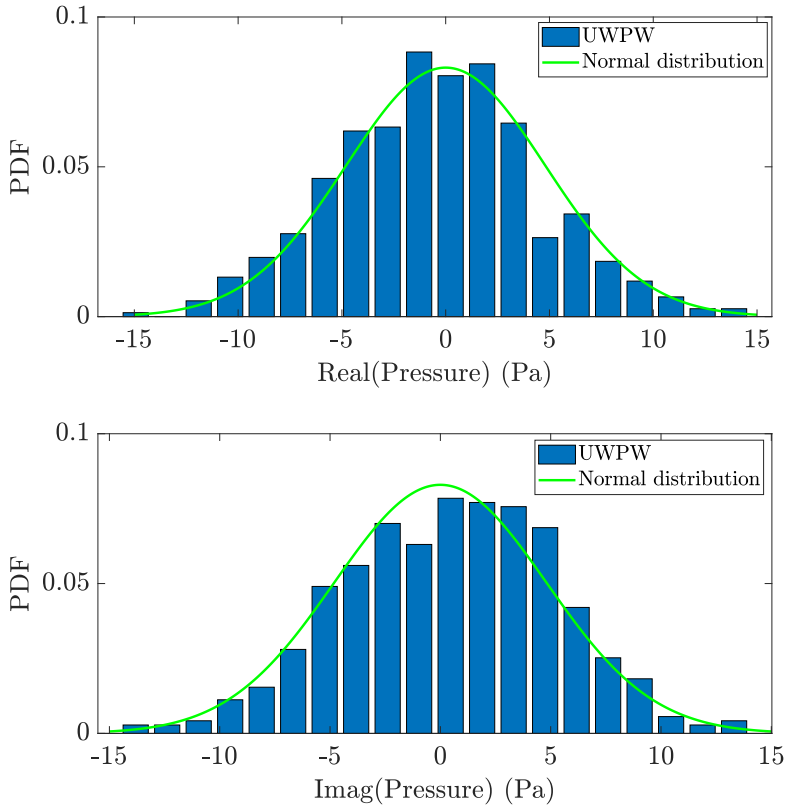

FIG. 5. (color online) Probability density function of the real and imaginary parts of synthesized surface pressure jump using 500 realizations at $\omega_r = 1$.

Figure 6 shows the averaged ASD distribution and its standard deviation based on 1000 calculations for a given number of realization at $\omega_r = 1$. It is evident from Figure 6 that dispersion of the averaged ASD of the synthesized pressure decreases as the number of realization increases. A similar trend can be seen for the standard deviation where the higher number of realizations results in a lower standard deviation. Above 50 realizations, the standard deviation of the ASD level is lower than 0.6 dB. Assuming a normal distribution for ASD of synthesized pressures, we have 95% confidence interval of ± 1.2 dB which indicates that for 95% of the samples, mean value lies within two standard deviations of the mean.

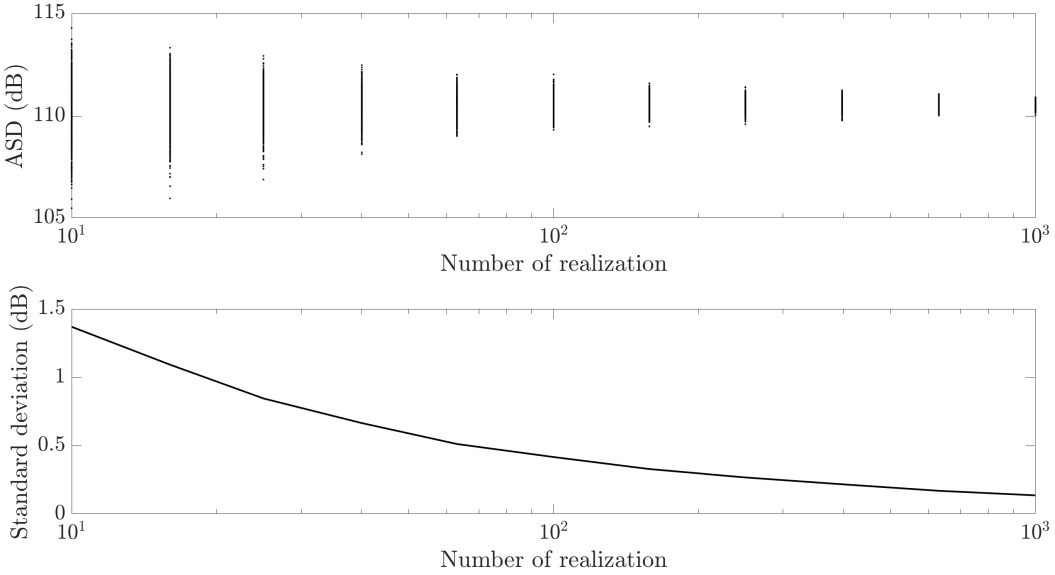

FIG. 6. Averaged ASD distribution (top) and its standard deviation (bottom) as a function of number of realization for 1000 samples (dB, ref. $4 \times 10^{-10}\mathrm{Pa}^2/\mathrm{Hz}$).

D. Sub-critical and super-critical gusts contribution

Gusts can be classified as sub- or super-critical, respectively corresponding to subsonic and supersonic phase speeds of their trace along the leading/trailing edge with respect to the incident mean flow (Amiet, 1975). For a given flow condition, the Graham's parameter of less than or greater than unity corresponds respectively to sub-critical or super-critical pressure gusts. Figure 7 highlights the contributions of sub-critical and super-critical gusts to the surface pressure jump. It can be observed that at low frequencies ($\omega_r \leq 4$) the super-critical gust have almost no contribution to the surface pressure jump and it is sufficient to only consider the sub-critical gust contribution. This fact can also be seen in Figure 2 (c) where at low frequency ($\omega_r \leq 4$ or $K_x \leq 13$ m^{-1}) contribution of super-critical gust is confined to the triangular region $R_1 = \{(K_x, k_y) \mid 0 \leq K_x \leq 13,\ 0 \leq k_y \leq (MK_x/\beta)\}$ while this region accounts only for

a small portion of the total contribution at this low frequency range in the entire region of $R = \{(K_x, k_y) \mid 0 \leq K_x \leq 13,\ 0 \leq k_y \leq 10\}$ where most of the wavenumbers are located in the sub-critical region.

According to Figure 2 (c), contributions of both sub-critical and super-critical gusts are equally important in the frequency range of $4 < \omega_r < 100$. At $\omega_r \approx 30$ or $K_x \approx 100$ m^{-1} they have the same contributions to the surface pressure field. For $\omega_r \geq 100$ the super-critical gust contributions dominate and there is no need to include sub-critical gust. This is consistent with the results in Figure 2 (c) where above this reduced frequency (corresponding to $K_x \approx 328$ m^{-1}) the wavenumbers located above the dashed line in the region of $\Theta < 1$ have almost zero contribution to the predicted surface pressure jump.

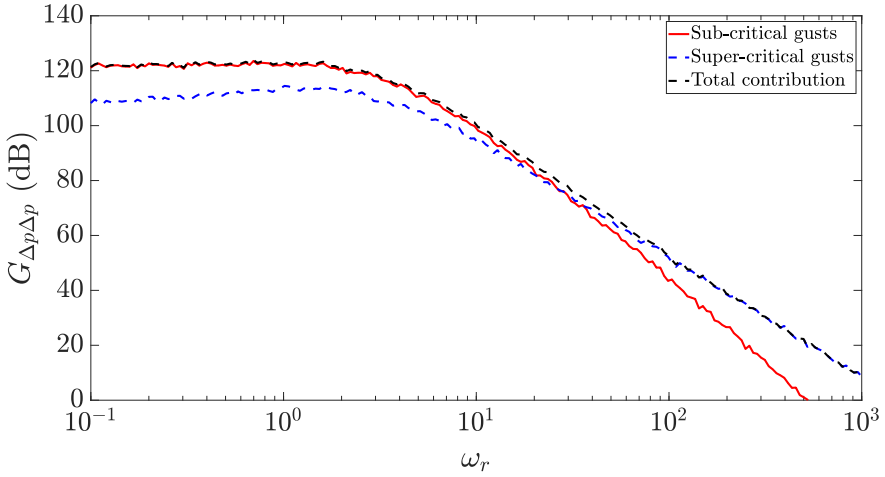

FIG. 7. (color online) Contributions of sub- and super-critical gusts to the surface pressure jump as a function of reduced frequency, (dB, ref. $4 \times 10^{-10}\text{Pa}^2/\text{Hz}$).

E. Verification and validation

To validate the surface pressure jump produced by the proposed method, the predicted pressure difference spectra at chordwise locations, $x/b = 0.05$, $x/b = 0.08$ and $x/b = 0.12$ are compared with experimental data measured by Mish and Devenport (2006a) in Figure 8. A NACA0015 with a chord of $0.610\,\mathrm{m}$ and span of $1.83\,\mathrm{m}$ at zero angle of attack has been considered with the turbulence parameters given in Table 1. $G_{\Delta p \Delta p}$ is the ASD of the surface pressure jump. It should be noted that in the work by Mish and Devenport (2006a), $G_{\Delta p \Delta p}$ was normalized by q^2, where q is the free-stream dynamic pressure ($q = 1/2\rho U_\infty^2$). Due to the proximity of the measurement locations to the leading edge, the modified von Karman spectrum has been implemented. Figure 8 shows that the present results are in excellent agreement with the measured shape and level of the spectra for $\omega_r \leq 20$. It can be observed that at low frequencies ($\omega_r \leq 2$) the spectrum level is almost constant and has its highest value over the entire frequency range. At these low frequencies, the sub-critical wavenumbers dominate the surface pressure response (as shown in Figure 2 (c)). Although sub-critical wavenumbers are often neglected in aeroacoustics, these results demonstrate that these wavenumbers must be considered when examining the force and vibroacoustic response of airfoils in turbulent flow.

The slope of the measured data decreases for $\omega_r > 20$. The divergence of the predicted results from the experimental data at high frequencies could be attributed to the pressure signatures of the large scale eddies convecting past the leading edge. This can be explained by the inner-outer scale interaction model developed by Mathis *et al.* (2009) that demonstrates large scale fluctuations in the outer region of the boundary layer have an amplitude and phase modulating effect on the inner scale fluctuations, wall shear stress and pressures. This modulation effect was also demonstrated

by Dogan *et al.* (2016) to occur for free stream turbulence convecting over turbulent boundary layers. Further, when the turbulent boundary layer develops over the airfoil surface, it induces pressure fluctuations which affect the high frequency response. As the boundary layer thickness increases by moving away from the leading edge, this affect is more profound at larger chordwise locations as shown in Figure 8. The spike in the measured data at high frequency was reported to be related to resonance within the microphone mounting hole (Mish and Devenport, 2006a).

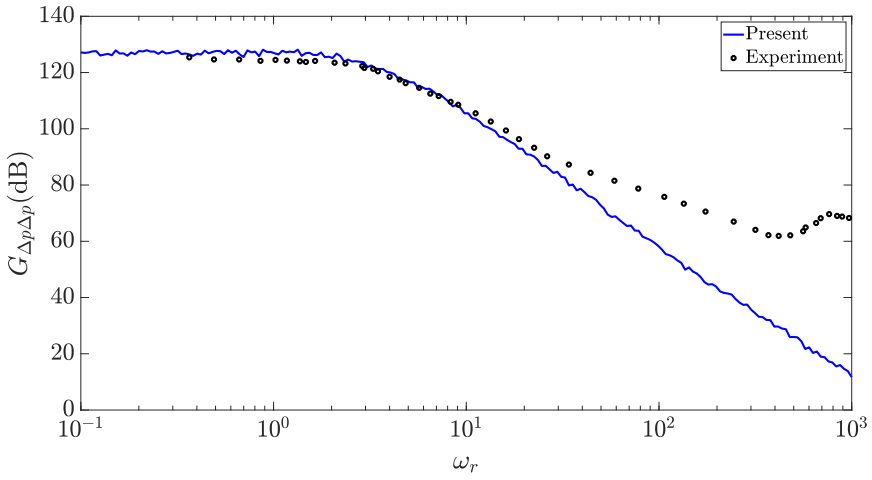

(a)

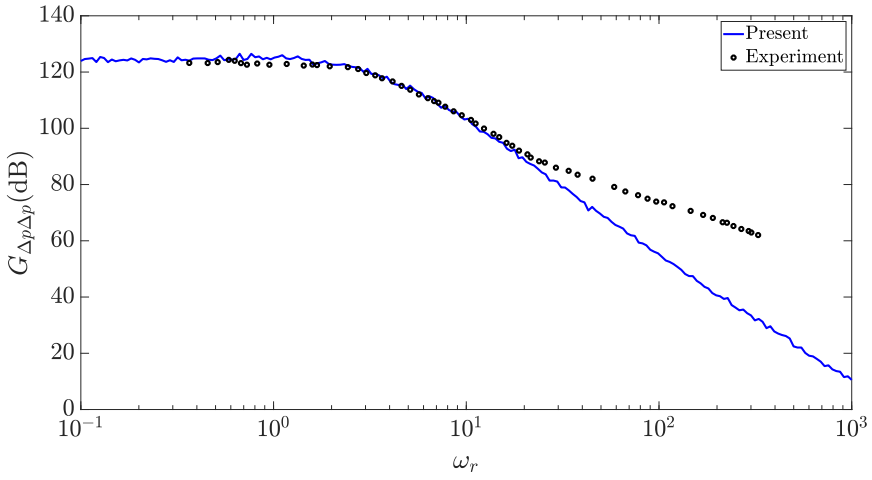

(b)

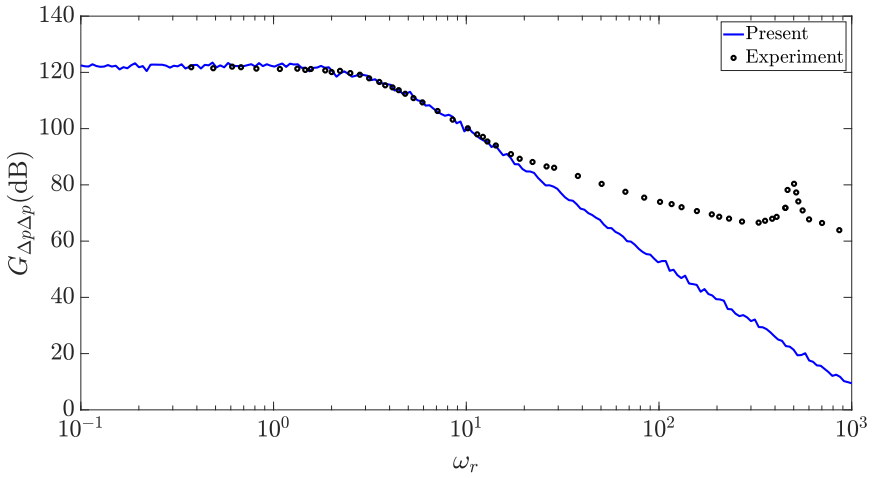

(c)

FIG. 8. (color online) Comparison between measured and predicted pressure difference spectral level for NACA0015 at (a) $x/b = 0.05$, (b) $x/b = 0.08$ and (c) $x/b = 0.12$ (dB, ref. $4 \times 10^{-10}\text{Pa}^2/\text{Hz}$).

To further validate the proposed method, the NACA0012 airfoil with a chord of $0.230\,\text{m}$ and span of $0.530\,\text{m}$, which was tested by Paterson and Amiet (1976), has been considered. Figure 9 shows a comparison between numerical results using the UWPW technique and experimental data for the airfoil chordwise unsteady surface pressure distribution at zero angle of attack. The prediction has been performed for different flow speeds at 400 Hz and 2000 Hz. The von Karman spectrum along with the turbulence parameters given in Table 1 were implemented. As can be seen, numerical results are in very good agreement with experimental data. The theoretical predictions using Amiet's theory is also included (Paterson and Amiet, 1976). The results indicate a strong increase in unsteady pressure near the leading edge. The surface pressure decreases moving away from the leading edge. It can also be observed that the spectrum level increases with an increase in flow speed. Figures 8 and 9 show that the proposed method can accurately predict the surface pressure at different location on the airfoil surface as well as at different frequencies.

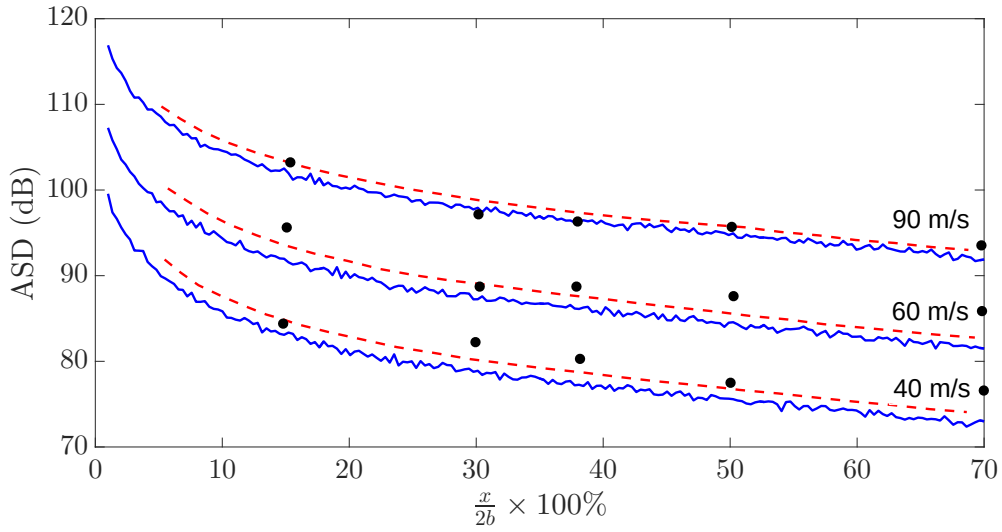

(a) 400 Hz

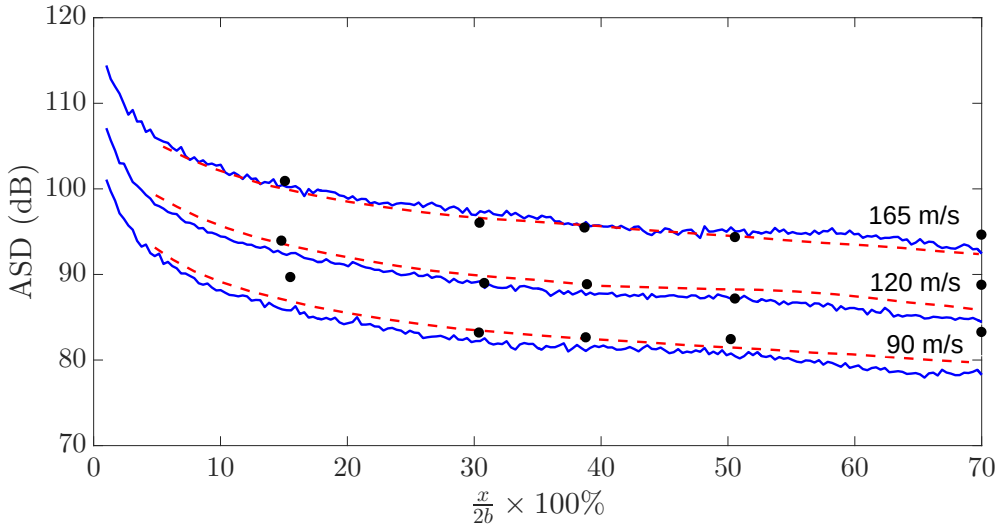

(b) 2000 Hz

FIG. 9. (color online) Comparison between measured and predicted auto spectrum density of surface pressure for a NACA0012 at (a) 400 Hz and (b) 2000 Hz. Present results (solid line), analytical results (dashed line) and experiment (Paterson and Amiet, 1976) (solid circle), (dB, ref. $4 \times 10^{-10}\mathrm{Pa}^2/\mathrm{Hz}$).

F. Unsteady force calculation

The unsteady force caused by turbulence ingestion has been studied by several investigators in the past (Anderson *et al.*, 2015; Jiang *et al.*, 1994). In this section unsteady force acting on the

NACA0015 airfoil (Case 1) due to the incoming turbulence is computed. A flat plate representing the airfoil was meshed with more grid points close to the leading edge to capture the variation of the surface pressure jump at the locations close to the leading edge. To estimate the unsteady force, realizations of surface pressure jump were initially obtained at each node on the surface. Figure 10 shows color maps of a realization of the surface pressure jump at frequencies of 10 Hz, 100 Hz, 300 Hz and 500 Hz. As expected, the highest values of the surface pressure occur at the leading edge and the pressure level monotonically decreases for the locations further away from leading edge, this was also observed in Figure 9. Moreover, it can be seen from these color maps that the pressure level reduces as frequency increases. This is also consistent with the results in Figure 8. Once enough realizations of the surface pressure jump are generated, Equation 28 can be used to calculate realizations of unsteady force by integrating the corresponding realization of pressure jump over the surface area. Finally, the unsteady force was computed from ensemble average over different realizations. The predicted force using the UWPW technique is compared with an analytical prediction described in the Appendix. Figure 11 shows that the present prediction is very close to the analytical results. Different realizations of the force are also included in the figure (in gray lines) which shows how a single realization of the response differs significantly from the final response obtained by ensemble average of all the realizations as shown by solid blue line.

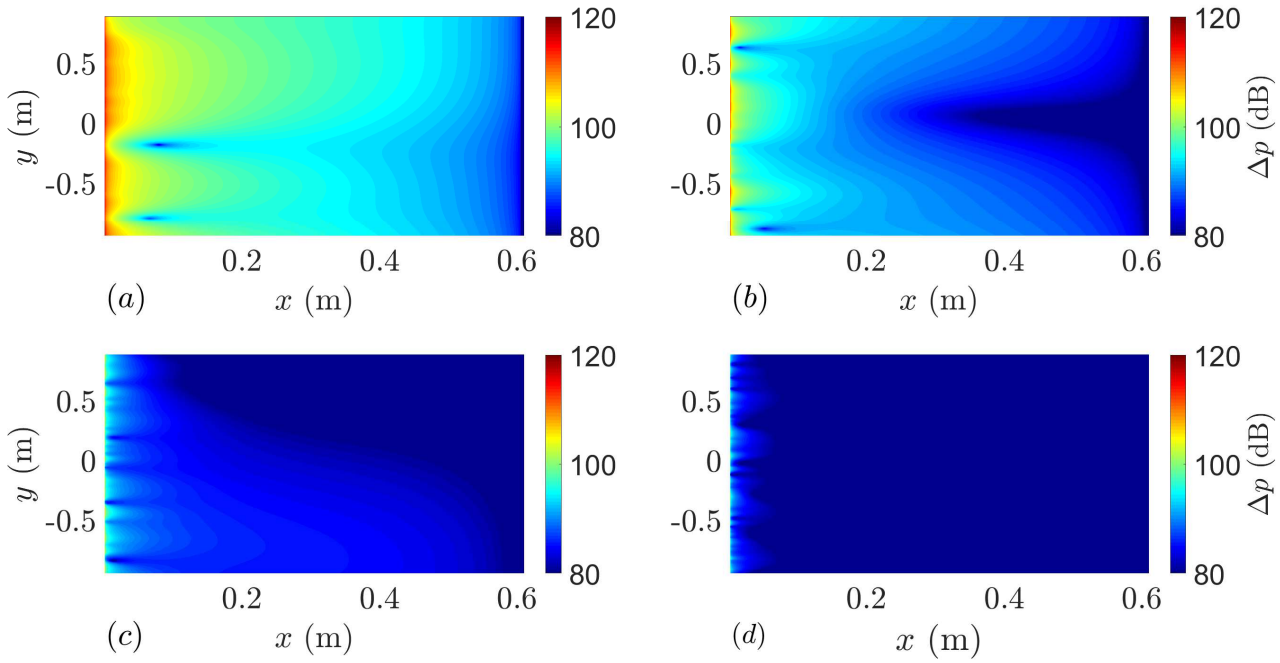

FIG. 10. (color online) A realization of the surface pressure jump on a flat plate representing the NACA0015 airfoil (flow direction is from left to right) at four distinct frequencies of (a) 10 Hz, (b) 100 Hz, (c) 300 Hz and (d) 500 Hz, (dB ref. 2×10^{-5} Pa).

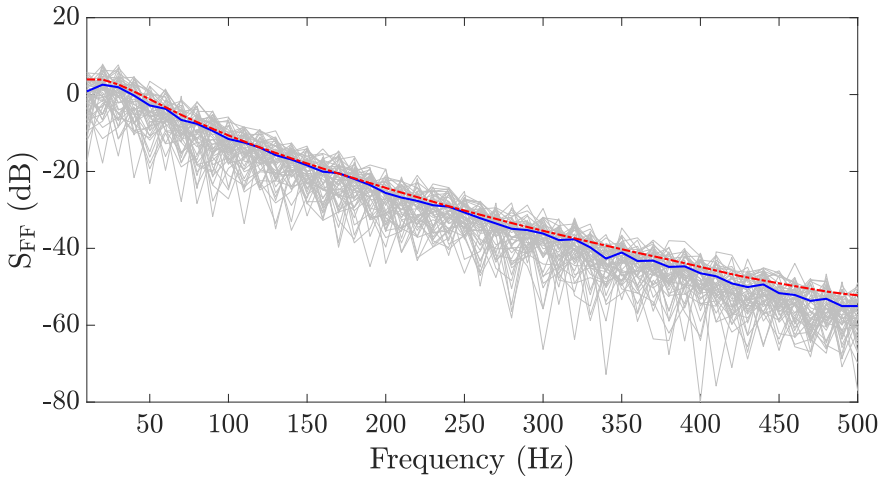

FIG. 11. (color online) ASD of unsteady force predicted using the UWPW technique for 50 realizations (gray lines), using the average of 50 realizations (blue solid line) as well as predicted analytically (red dashed line) for the NACA0015, (dB, ref. 1 N/Hz).

V. CONCLUSIONS

In this work, we proposed a numerical technique to simulate the surface pressure induced by incoming turbulence. The surface pressure jump was expressed as a set of uncorrelated wall pressure plane waves with their amplitudes determined by the incoming upwash velocity spectrum and the airfoil aeroacoustic transfer function. To achieve a good estimation of the surface pressure jump, criteria for cut-off wavenumber and wavenumber resolution were established. Contributions of sub- and super-critical gust to the surface pressure were examined. It was found that the sub-critical gust contribution is dominant at low frequency while the super-critical gust contribution dominates at high frequencies. The surface pressure jump predicted from an ensemble average of the different realizations was compared with numerical and experimental results, showing very good agreement. To demonstrate an application of the proposed technique, the unsteady force due to incoming turbulence excitation on an airfoil was calculated. The numerical prediction agreed well with analytical results. One of the main advantages of the proposed technique is that the surface pressures simulated by the UWPW technique are deterministic and they can be applied as load to an element-based vibroacoustic solver to obtain structural and acoustic responses of airfoils. In the future study this advantage of the proposed method will be exploited to predict and analyze vibroacoustic response of a structure due to stochastic excitation (incident turbulence) using deterministic element-based methods such as the finite element and boundary element methods.

ACKNOWLEDGMENTS

The first author gratefully acknowledges financial support from the Australian Government through the Australian Research Council's Discovery Early Career Project funding scheme (project DE190101412).

APPENDIX

The analytical model used to estimate the force produced on an airfoil in turbulent flow is presented here. The analytical model is based on the aeroacoustic scattering model originally presented by Amiet (Amiet, 1975) and later extended by Roger and Moreau to include trailing edge backscatter (Roger and Moreau, 2010). The turbulence ingestion noise model derived by Roger and Moreau is given by:

$$S_{pp}\left(\mathbf{x},\omega\right) = \left(\frac{k_a \rho_0 b x_3}{S_0^2}\right)^2 U_0 \int_{-\infty}^{\infty} \Phi_{ww}\left(\frac{\omega}{U_c}, k_y\right) \frac{\sin^2\left(d\left(\frac{k_a x_2}{S_0} - k_y\right)\right)}{\left(\frac{k_a x_2}{S_0} - k_y\right)^2} \times \left|\mathcal{L}_{\text{TI}}\left(x_1, \frac{\omega}{U_0}, k_y\right)\right|^2 \mathrm{d}\, k_y \tag{30}$$

where $S_{pp}\left(\mathbf{x},\omega\right)$ is the power spectral density of the far-field sound at angular frequency ω and field point $\mathbf{x}$. k_a is the acoustic wavenumber and ρ_0 is the speed of sound and density of the fluid at rest. x_i is the i^{th} component of the far-field position vector $\mathbf{x}$. $S_0^2 = x_1^2 + \beta^2\left(x_2^2 + x_3^2\right)$ is the distance from the coordinate system origin at the leading edge to the far-field location $\mathbf{x}$, with $\beta^2 = 1 - M^2$, M being the Mach number. The airfoil span and chord length are given respectively by $2d$ and $2b$. $\Phi_{ww}\left(\frac{\omega}{U_c}, k_y\right)$ is the upwash spectrum and is a function of convective wavenumber $k_c = \frac{\omega}{U_c}$, where U_c is the convection velocity of the upwash disturbance, and the

spanwise wavenumber k_y. $\mathcal{L}_{\text{TI}}$ is the aeroacoustic transfer function. The present analytical work uses the von Karman spectrum modified to account for rapid distortion of turbulence structures by the leading edge to approximate the upwash spectrum.

The airfoil can be discretised into a number of strips, N_s, with the total far-field sound over all strips given by:

$$S_{pp}\left(\mathbf{x},\omega\right) = \sum_{s=1}^{N_s}\left[\left(\frac{k_a\rho_0 b x_{s3}}{S_{s0}^2}\right)^2 U_{s0}\int_{-\infty}^{\infty}\Phi_{ww}\left(\frac{\omega}{U_{s0}},k_y\right) \frac{\sin^2\left(d_s\left(\frac{k_a x_{s2}}{S_{s0}}-k_y\right)\right)}{\left(\frac{k_a x_{s2}}{S_{s0}}-k_y\right)^2}\times\left|\mathcal{L}_{\text{TI}}\left(x_{s1},\frac{\omega}{U_{s0}},k_y\right)\right|^2 \mathrm{d}\,k_2\right] \tag{31}$$

where the subscript s denotes the strip-wise value, with d_s representing the half strip span. Equation (31) is referred to as the direct strip-wise approach and was found by Christophe et al. (Christophe *et al.*, 2009) to diverge from the correct result as strip size decreases. Christophe et al. (Christophe *et al.*, 2009) proposed an alternate strategy for strip-wise turbulence ingestion noise modelling that they called the 'inverse' strip-wise method. The inverse strip-wise technique calculates the sound from each strip by representing the strip-wise half span d_s as the difference of two large span values $d_s = d_L - \left(d_L - d_s\right),\ d_L >> d_s$ to give:

$$S_{pp}\left(\mathbf{x},\omega\right) = \sum_{s=1}^{N_s}\left[\left(\frac{k_a\rho_0 b x_{s3}}{S_{s0}^2}\right)^2 U_{s0}\int_{-\infty}^{\infty}\Phi_{ww}\left(\frac{\omega}{U_{s0}},k_y\right) \left(\frac{\sin^2\left(d_L\left(\frac{k_a x_{s2}}{S_{s0}}-k_y\right)\right)}{\left(\frac{k_a x_{s2}}{S_{s0}}-k_y\right)^2}-\frac{\sin^2\left(\left(d_L-d_s\right)\left(\frac{k_a x_{s2}}{S_{s0}}-k_y\right)\right)}{\left(\frac{k_a x_{s2}}{S_{s0}}-k_y\right)^2}\right) \times\left|\mathcal{L}_{\text{TI}}\left(x_{s1},\frac{\omega}{U_{s0}},k_y\right)\right|^2 \mathrm{d}\,k_y\right] \tag{32}$$

In the current work, d_L is set equal to the total half span d. The inverse strip-wise technique is often combined with the large aspect ratio approximation to equation (31). For infinite span

457 airfoils, only gusts which are parallel to the leading edge generates pressure waves that radiate to
458 the far-field as sound. However, the current application is to estimate the total force on the airfoil
459 and hence evanescent components may be significant. For this reason, equation (32) retains the
460 integral over spanwise wavenumbers.

461 As the application of this technique is focused on force prediction, the radiation of pressure
462 waves to the far-field is not required. Propagation of pressure waves from the leading edge to the
463 far-field is included in equation (32) via a dipole radiation function and by propagation terms in
464 the transfer function $\mathcal{L}_{\text{TI}}$. The first step in removing the far-field radiation terms from equation
465 (32) is to extract the dipole radiation function. The far-field sound produced by a unit harmonic
466 point force oriented in the wall-normal, x_{s3} direction, can be expressed as:

$$S_{pp}\left(\mathbf{x},\omega\right) = \left(\frac{k_a x_{s3}}{4\pi S_0^2}\right)^2 \tag{33}$$

467 Removing this radiation component and aeroacoustic transfer function propagation terms from
468 equation(32) gives the following expression for the total force on the airfoil due to interaction with
469 the turbulence stream:

$$\begin{aligned} S_{ff}\left(\mathbf{x},\omega\right) = \sum_{s=1}^{N_s} \Bigg[& \left(4\pi\rho_0 b\right)^2 U_{s0} \int_{-\infty}^{\infty} \Phi_{ww}\left(\frac{\omega}{U_{s0}}, k_y\right) \\ & \left(\frac{\sin^2\left(d\left(\frac{k_a x_{s2}}{S_{s0}} - k_y\right)\right)}{\left(\frac{k_a x_{s2}}{S_{s0}} - k_y\right)^2} - \frac{\sin^2\left(\left(d-d_s\right)\left(\frac{k_a x_{s2}}{S_{s0}} - k_y\right)\right)}{\left(\frac{k_a x_{s2}}{S_{s0}} - k_y\right)^2} \right) \\ & \times \left|\mathcal{L}_{\text{TI}}\left(\frac{\omega}{U_{s0}}, k_y\right)\right|^2 \mathrm{d}\, k_y \Bigg] \end{aligned} \tag{34}$$

470 The transfer function $\mathcal{L}_{\text{TI}} = \mathcal{L}_1 + \mathcal{L}_2$, where $\mathcal{L}_1$ represents the principal scattering from the airfoil
471 leading edge and $\mathcal{L}_2$ accounts for back-scattering from the airfoil trailing edge. The transfer func-

tions for supercritical wavenumbers derived by Roger and Moreau, with the far-field propagation terms removed, are given by:

$$\mathcal{L}_1 = -\frac{1}{\pi}\sqrt{\frac{2}{\left(K_x^* + \beta^2\bar{\kappa}\right)\bar{\kappa}}}\,\mathrm{e}^{-\mathrm{i}\,\Theta_2}\,\mathfrak{F}\left[2\bar{\kappa}\right] \tag{35}$$

$$\mathcal{L}_2 = \frac{e^{-\mathrm{i}\,\Theta_2}}{\pi\bar{\kappa}\sqrt{2\pi\left(K_x^* + \beta^2\bar{\kappa}\right)}} \times \left(\mathrm{i}\left(1 - \mathrm{e}^{2\,\mathrm{i}\,\bar{\kappa}}\right) - (1+\mathrm{i})\left(\mathfrak{F}\left[4\bar{\kappa}\right] - \mathrm{e}^{2\,\mathrm{i}\,\bar{\kappa}}\,\sqrt{2}\mathfrak{F}\left[2\left(\bar{\kappa}\right)\right]\right)\right) \tag{36}$$

where $K_x^* = K_x b$, $\bar{\kappa} = \sqrt{\bar{\mu}^2 - \frac{k_y^{*2}}{\beta^2}}$, $\bar{\mu} = \frac{k_a b}{\beta^2} = \frac{K_x^* M_0}{\beta^2}$, $\Theta_2 = \bar{\mu}M_0 - \frac{\pi}{4}$ and $k_y^* = k_y b$. The transfer functions for subcritical wavenumbers are given by:

$$\mathcal{L}_1 = -\frac{1}{\pi}\sqrt{\frac{2}{\left(K_x^* + \mathrm{i}\,\beta^2\bar{\kappa}'\right)\mathrm{i}\,\bar{\kappa}'}}\,\mathrm{e}^{-\mathrm{i}\,\Theta_2}\,\mathfrak{F}\left[2\,\mathrm{i}\,\bar{\kappa}'\right] \tag{37}$$

$$\mathcal{L}_2 = \frac{\mathrm{e}^{-\mathrm{i}\,\Theta_2}}{\pi\bar{\kappa}'\sqrt{2\pi\left(K_x^* + \mathrm{i}\,\beta^2\bar{\kappa}'\right)}} \times \left(1 - \mathrm{e}^{-2\bar{\kappa}'} - \mathrm{erf}\left(\sqrt{4\bar{\kappa}'}\right) + 2\,\mathrm{e}^{-2\bar{\kappa}'}\,\sqrt{-\mathrm{i}}\mathfrak{F}\left[2\left(\mathrm{i}\,\bar{\kappa}'\right)\right]\right) \tag{38}$$

where $\bar{\kappa}' = \sqrt{\frac{k_y^{*2}}{\beta^2} - \bar{\mu}^2}$.

REFERENCES

Abramowitz, M., and Stegun, I. A. (**1948**). *Handbook of mathematical functions with formulas, graphs, and mathematical tables*, **55** (US Government printing office).

Amiet, R. . (**1976**a). "Noise due to turbulent flow past a trailing edge," J. Sound Vib. **47**(3), 387–393.

Amiet, R. (**1975**). "Acoustic radiation from an airfoil in a turbulent stream," J. Sound Vib. **41**(4), 407–420.

Amiet, R. (**1978**). "Effect of the incident surface pressure field on noise due to turbulent flow past a trailing edge," J. Sound Vib. **57**(2), 305–306.

Amiet, R. K. (**1976**b). "High frequency thin-airfoil theory for subsonic flow," AIAA J. **14**(8), 1076–1082.

Anderson, J. M., Catlett, M. R., and Stewart, D. O. (**2015**). "Modeling rotor unsteady forces and sound due to homogeneous turbulence ingestion," AIAA J. **53**(1), 81–92.

Ayton, L. J., and Chaitanya, P. (**2017**). "Analytical and experimental investigation into the effects of leading-edge radius on gust–aerofoil interaction noise," J. Fluid Mech. **829**, 780–808.

Ayton, L. J., and Peake, N. (**2016**). "Interaction of turbulence with the leading-edge stagnation point of a thin aerofoil," J. Fluid Mech. **798**, 436–456.

Bechara, W., Bailly, C., Lafon, P., and Candel, S. M. (**1994**). "Stochastic approach to noise modeling for free turbulent flows," AIAA J. **32**(3), 455–463.

Brooks, T. (**1981**). "Trailing edge noise prediction using Amiet's method," J. Sound Vib. **77**(3), 437–439.

Christophe, J. (**2011**). "Application of hybrid methods to high frequency aeroacoustics," Université Libre de Bruxelles .

Christophe, J., Anthoine, J., and Moreau, S. (**2009**). "Amiet's theory in spanwise-varying flow conditions," AIAA J. **47**, 788–790.

de Santana, L. D., Schram, C., and Desmet, W. (**2015**). "Airfoil noise prediction from 2D3C PIV data," 21st AIAA/CEAS Aeroacoustics Conference, Dallas, Texas, 22-26 June **No. 2203**.

505 Devenport, W. J., Staubs, J. K., and Glegg, S. A. (**2010**). "Sound radiation from real airfoils in
506 turbulence," J. Sound Vib. **329**(17), 3470–3483.

507 Dogan, E., Hanson, R., and Ganapathisubramani, B. (**2016**). "Interactions of large-scale free-
508 stream turbulence with turbulent boundary layers," J. Fluid Mech. 1–29.

509 Filotas, L. (**1969**). "Response of an infinite wing to an oblique sinusoidal gust: a generalization of
510 sears' problem," NASA Special Publication **207**(No. 231).

511 Glegg, S. A., and Devenport, W. J. (**2010**). "Panel methods for airfoils in turbulent flow," J. Sound
512 Vib. **329**(18), 3709–3720.

513 Hunt, J. (**1973**). "A theory of turbulent flow round two-dimensional bluff bodies," J. Fluid Mech.
514 **61**(4), 625–706.

515 Hutcheson, F. V., Brooks, T. F., and Stead, D. J. (**2012**). "Measurement of the noise resulting from
516 the interaction of turbulence with a lifting surface," Int. J. Aeroacoust. **11**(5-6), 675–700.

517 Jiang, C., Chang, M., and Liu, Y. (**1994**). "The effect of turbulence ingestion on propeller broad-
518 band forces," Naval Hydrodynamics, 19th Symposium; 23-28 August 1992; Seoul, Korea. .

519 Karimi, M., Croaker, P., Maxit, L., Robin, O., Skvortsov, A., Marburg, S., and Kessissoglou, N.
520 (**2020**). "A hybrid numerical approach to predict the vibrational responses of panels excited by
521 a turbulent boundary layer," J. Fluids Struct. **92**, 102814.

522 Karimi, M., Croaker, P., Skvortsov, A., Moreau, D., and Kessissoglou, N. (**2019**a). "Numerical
523 prediction of turbulent boundary layer noise from a sharp-edged flat plate," Int. J. Numer. Meth.
524 Fl. **90**, 522–543.

525 Karimi, M., Maxit, L., Croaker, P., Robin, O., Skvortsov, A., Marburg, S., Atalla, N., and Kessis-
526 soglou, N. (**2019**b). "Analytical and numerical prediction of acoustic radiation from a panel

527 under turbulent boundary layer excitation," J. Sound Vib. .

528 Kraichnan, R. H. (**1970**). "Diffusion by a random velocity field," Phys. Fluids **13**(1), 22–31.

529 Lysak, P. D. (**2001**). "A model for the broadband unsteady forces in a marine propulsor due to
530 inflow turbulence," Ph.D. thesis, Pennsylvania State University.

531 Mathis, R., Hutchins, N., and Marusic, I. (**2009**). "Large-scale amplitude modulation of the small-
532 scale structures in turbulent boundary layers," J. Fluid Mech. **628**, 311–337.

533 Maxit, L. (**2016**). "Simulation of the pressure field beneath a turbulent boundary layer using real-
534 izations of uncorrelated wall plane waves," J. Acoust. Soc. Am. **140**(2), 1268–1285.

535 Mish, P. F. (**2001**). "Mean loading and turbulence scale effects on the surface pressure fluctuations
536 occurring on a NACA 0015 airfoil immersed in grid generated turbulence," Phd thesis, Virginia
537 Tech.

538 Mish, P. F., and Devenport, W. J. (**2003**). "An experimental investigation of unsteady surface
539 pressure on an airfoil in turbulence," Final report to NASA Langley under grant NAG-1-2272 .

540 Mish, P. F., and Devenport, W. J. (**2006**a). "An experimental investigation of unsteady surface
541 pressure on an airfoil in turbulence-part 1: Effects of mean loading," J. Sound Vib. **296**(3), 417–
542 446.

543 Mish, P. F., and Devenport, W. J. (**2006**b). "An experimental investigation of unsteady surface
544 pressure on an airfoil in turbulence-part 2: Sources and prediction of mean loading effects," J.
545 Sound Vib. **296**(3), 447–460.

546 Moreau, S., Christopher, J., and Roger, M. (**2008**). "Les of the trailing-edge flow and noise of a
547 naca0012 airfoil near stall," in *Proceedings of the Summer Program*, pp. 317–329.

548 Moreau, S., and Roger, M. (**2007**). "Competing broadband noise mechanisms in low-speed axial
549 fans," AIAA Journal **45**(1), 48–57.

550 Paterson, R., and Amiet, R. (**1976**). "Acoustic radiation and surface pressure characteristics of an
551 airfoil due to incident turbulence," 3rd Aeroacoustics Conference, Palo Alto, California, 20-23
552 July **No. 76-571**.

553 Roger, M., and Moreau, S. (**2010**). "Extensions and limitations of analytical airfoil broadband
554 noise models," Int. J. Aeroacoust. **9**(3), 273–305.

555 Santana, L. D., Christophe, J., Schram, C., and Desmet, W. (**2016**). "A rapid distortion theory
556 modified turbulence spectra for semi-analytical airfoil noise prediction," J. Sound Vib. **383**, 349–
557 363.